



# Modeling and analysis of LiFePO<sub>4</sub>/Carbon battery considering two-phase transition during galvanostatic charging/discharging



Xueyan Li<sup>a</sup>, Meng Xiao<sup>b</sup>, Song-Yul Choe<sup>c,\*</sup>, Won Tae Joe<sup>d</sup>

<sup>a</sup> Mechanical Engineering, 1418 Wiggins Hall, Auburn Univ., AL 36849, USA

<sup>b</sup> Mechanical Engineering, 1418 Wiggins Hall, Auburn Univ., AL 36849, USA

<sup>c</sup> Mechanical Engineering, 1418 Wiggins Hall, Auburn Univ., AL 36849, USA

<sup>d</sup> Battery R&D, LG Chem Research Park, Daejeon, 305-738, South Korea

## ARTICLE INFO

### Article history:

Received 1 October 2014

Received in revised form 1 December 2014

Accepted 8 December 2014

Available online 12 December 2014

## ABSTRACT

Batteries with lithium iron phosphate (LFP) cathode and carbon anode have shown various advantages over those with other chemistries, but the plateau and path dependence caused by the two-phase transition taking place during charging and discharging make it difficult to estimate the states of battery. Thus, based on electrochemical principles we propose a new reduced order model that has been validated against experimental data obtained during galvanostatic charging/discharging.

The mechanism of the two-phase transition during lithiation and delithiation in LFP particles is approximated using a shrinking core with a moving interface between the two phases and is described by modified diffusion equations that take into account multiple layers formed within LFP particles. The shrinking core model is integrated into a cell model developed previously, which is used to analyze the path dependence at different load profiles.

The results show that the model is capable of representing the characteristics of the plateau and path dependence. Particularly, the available charge at a certain State of Charge (SOC) varies dependent upon paths to reach the SOC. When an initial SOC is reached by discharging, the cell can accept more charges during charging, while when an initial SOC is reached by charging, more charge will be available during discharging.

© 2014 Elsevier Ltd. All rights reserved.

## 1. Review of model with LFP cathode

There has been impressive research focusing on LFP since 1997 [1]. As a promising cathode material, LiFePO<sub>4</sub> (LFP) has been widely used in commercial Li-ion batteries because of excellent safety by its electrochemical and thermal stability, and high rate capacity enhanced especially using nanoparticles in addition to a good cycle life and low cost. All these characteristics enable LFP to be the potential material for applications in electric and hybrid electric vehicles.

Modeling efforts have been made to design estimation algorithms or to understand detailed mechanism of ion transport as well as intercalation and deintercalation process along with material properties. The models widely used for Li-ion battery can be classified into two categories: Electrochemical thermal model based on physical principles, and electric equivalent circuit

model (EECM) composing of a voltage source and electric circuit components. Typically, state-of-charge (SOC) is calculated using its relationship with open circuit voltage (OCV) that is estimated from the measured terminal voltage. However, the extreme flat charge/discharge voltage curve of Li ion batteries with LFP chemistry makes it difficult to estimate state-of-charge (SOC). Therefore, a model is needed to predict the SOC in addition to other control purposes. Current electrochemical thermal models using partial differential equations are computationally intensive and cannot be used for real time applications. Therefore, a reduced order model is needed for control purpose that reflects two phase transition effects.

Electrochemical thermal models usually involve ion transport between electrodes, chemical reactions at the electrode/electrolyte interface, and ion diffusion and intercalation as well as deintercalation in solid particles. The ion diffusion and distribution dynamics in cathode particles is dependent upon chemistry. For LFP, the lithium ion insertion/extraction reaction takes place through a narrow mono-phase, a two-phase and another narrow mono-phase process. The two-phase process is the most dominant one that occurs between lithium deficient phase ( $\alpha$  phase:

\* Corresponding author. Tel.: +1 334 844 3329, Fax: +1 334 844 3307.

E-mail addresses: [xzl0017@auburn.edu](mailto:xzl0017@auburn.edu) (X. Li), [mzx0001@auburn.edu](mailto:mzx0001@auburn.edu) (M. Xiao), [choe@auburn.edu](mailto:choe@auburn.edu) (S.-Y. Choe), [wontaejoe@lgchem.com](mailto:wontaejoe@lgchem.com) (W.T. Joe).

### Nomenclatures

|                  |   |
|------------------|---|
| A                | sandwich area of the cell ( $\text{cm}^2$ )   |
| $a_s$            | specific surface area of electrode ( $\text{cm}^{-1}$ )   |
| $c$              | ion concentration in solid phase ( $\text{mol L}^{-1}$ )  |
| $D$              | diffusion coefficient in electrode ( $\text{cm}^2 \text{s}^{-1}$ )  |
| $F$              | Faraday constant ( $96,487 \text{ C mol}^{-1}$ )  |
| $I$              | current of the cell (A)   |
| $i$              | current density ( $\text{A cm}^{-2}$ )  |
| $i_0$            | exchange current density of intercalation ( $\text{A cm}^{-2}$ )  |
| $j^{Li}$         | reaction rate of intercalation ( $\text{A cm}^{-3}$ )   |
| $L$              | thickness of the micro cell (cm)  |
| OCV              | open circuit voltage (V)  |
| $Q$              | capacity of the cell (Ah)   |
| $Q_{\text{max}}$ | maximum capacity of the cell (Ah)   |
| $q_{\text{ave}}$ | volume-averaged concentration flux ( $\text{mol cm}^{-4}$ )   |
| $R$              | resistance ( $\Omega \text{ cm}^2$ ) or universal gas constant ( $8.3143 \text{ J mol}^{-1} \text{ K}^{-1}$ )                           |
| $R_s$            | radius of spherical electrode particle (cm)   |
| $r$              | coordinate along the radius of electrode particle (cm) or location of the interface between $\alpha$ and $\beta$ phase in LFP particles |
| SOC              | state of charge   |
| $t$              | time (s)  |
| $t^0_+$          | transference number   |
| $U_{\text{equ}}$ | equilibrium potential (V)   |
| $V_t$            | terminal voltage of cell (V)  |

### Greek symbols

|               |  |
|---------------|--|
| $\alpha$      | transfer coefficient of reaction                                   |
| $\varepsilon$ | volume fraction  |
| $\varphi$     | electrical potential (V)   |
| $\eta$        | overpotential (V)  |
| $\kappa$      | ionic conductivity ( $\text{S cm}^{-1}$ )                          |
| $\kappa_D$    | concentration driven diffusion conductivity ( $\text{A cm}^{-1}$ ) |
| $\sigma$      | conductivity ( $\text{S cm}^{-1}$ )                                |

### Subscripts

|          |                               |
|----------|-------------------------------|
| ave      | average                       |
| cell     | single cell                   |
| e        | electrolyte phase             |
| max      | maximum                       |
| s        | solid phase (active material) |
| sep      | separator                     |
| surf     | Surface of electrode particle |
| $\alpha$ | $\alpha$ phase                |
| $\beta$  | $\beta$ phase                 |
| 0%       | 0% state of charge            |
| 100%     | 100% state of charge          |

### Superscripts

|     |           |
|-----|-----------|
| eff | effective |
|-----|-----------|

(XRD) and scanning electron microscopy (SEM) that individual nano particle (100 nm) is fully intercalated or fully deintercalated, which is explained using a domino-cascade model. This mechanism was manifested by Brunetti [5] by showing fully lithiated or fully delithiated particles at different nanoscale level (50–300 nm) using transmission electron microscopy (TEM) along with precession electron diffraction (PED). The studies above state that there exists a single phase. However, other researchers found out that there exist two phases in one primary particle. Weichert [6] observed formation of porous  $\text{FePO}_4$  (FP) layer on the surface of the LFP large single crystals (1.3  $\mu\text{m}$ ) after delithiation. Similarly, Zhu [7] investigated staging phase and phase transition in LFP with different sizes (50, 70, 200 nm) and found that a narrow interfacial zone present between LFP and FP decreases when particle size increases.

For secondary particles at cell level, shrinking core model is widely used to model the two phase transition in LFP micro-size particles that represent agglomerating nano-size primary particles. Considering the difference of the conductivity and diffusivity between the two phases, Srinivasan [8] proposed a shrinking core model that is used to describe the phase change, where the shell of one phase covers the core of the other phase. The model can represent ion diffusion inside of solid particles, and the moving of the interface between the two phases. Wang [9,10] improved the shrinking core model, assuming that both lithium ion concentration gradient and interface mobility are the driving forces for the two-phase transition. The rate capability is analyzed with different solid solutions and particle size of LFP.

Wheeler [11] proposed a LFP model based on sandwich structure that considers the phase-change diffusivity with a concentration-dependent solid diffusion coefficient. The model can represent the effect of carbon coating and inter-particle contacts with a spreading resistance. Without considering the two-phase transition process or the porous electrode, Safari [12] also proposed a model with an empirical equation that includes a diffusion coefficient dependent on the average concentration inside of a particle. The model also considers a resistive-reactant feature caused by the insolation of LFP materials. The results are capable of representing the asymmetry between the charge and discharge curves.

Srinivasan [13] showed that the behavior of LFP cells at a particular SOC depended on the path by which the SOC is reached, which is called path dependence of SOC. The mechanism of the phenomena is explained using a shrinking core model considering the cycling history that affects the diffusion length. Roscher's research [14] on load history dependent cell impedance is consistent with Srinivasan's description. In addition, effects of load history on power capability and available capacity are also analyzed. Safari [15] also proposed a model including the path dependence of the LFP electrode, but without considering phase transitions.

More and more researchers have experimentally proved the moving boundary theory. Phase transition and phase boundary propagation during delithiation in LFP particles is observed using electron energy loss spectroscopy [16,17]. The lithium ion diffusion coefficient measured by Churikov [18] shows its dependence on the ratio between two phases. However, there is no physical model available for LFP chemistry employing the moving boundary along with multiple layers to analyze path dependence yet. Therefore, we propose a reduced model for real time application of LFP cells, whose cathode is made of micro-size secondary particles. The model considers the two-phase transition, moving boundary, and multiple layers, which represents responses at both charging and discharging, and the path dependence of the LFP cathode.

$\text{Li}\alpha\text{FePO}_4$ ) and lithium rich phase ( $\beta$  phase:  $\text{Li}_{1-\beta}\text{FePO}_4$ ). Yamada [2] explained the existence of the mono-phase region and the reaction of the bi-phase region with experiments, and estimated nonstoichiometric parameters in the bi-phase region.

For primary particles, the phase transition in LFP is determined by crystal size. Chen [3] studies the phase transition mechanism by SEM on large LFP crystallites (0.2  $\mu\text{m}$ ). It turned out that lithium extraction takes place at the  $ac$  crystal surface and the boundary of two-phase moves in the direction of the  $a$ -axis. Delmas [4] found out by experiments using by X-ray Diffraction

**Table 1**

Summary of the governing equations for a full order model (FOM) and reduced order model of LMO cells.

| Equation description                    | Full order equations   | Reduced order equations  |
|---|--|--|
| Ion concentration in the solid phase    | $\frac{\partial c_s}{\partial t} = \frac{D_s}{r^2} \frac{\partial}{\partial r} \left( r^2 \frac{\partial c_s}{\partial r} \right)$ $\frac{1}{r} \frac{\partial c_s}{\partial r} \Big _{r=0} = 0$ $D_s \frac{\partial c_s}{\partial r} \Big _{r=R_s} = \frac{-j^{Li}}{a_s F}$   | $\frac{d}{dt} c_{s,ave} + 3 \frac{j^{Li}}{R_s a_s F} = 0$ $\frac{d}{dt} q_{ave} + 30 \frac{D_s}{R_s^2} q_{ave} + \frac{45}{2} \frac{j^{Li}}{R_s^2 a_s F} = 0$ $35 \frac{D_s}{R_s} (c_{s,surf} - c_{s,ave}) - 8 D_s q_{ave} = - \frac{j^{Li}}{a_s F}$ |
| Ohm's law in the solid phase            | $\frac{\partial}{\partial x} \left( \sigma^{eff} \frac{\partial \varphi_s}{\partial x} \right) - j^{Li} = 0$ $- \sigma^{eff} \frac{\partial \varphi_s}{\partial x} \Big _{x=0} = - \sigma^{eff} \frac{\partial \varphi_s}{\partial x} \Big _{x=L} = \frac{I}{A}$ $\frac{\partial \varphi_s}{\partial x} \Big _{x=L} = \frac{\partial \varphi_s}{\partial x} \Big _{x=L+L_{sep}} = 0$ | $a \quad \frac{\partial}{\partial x} \left( \frac{\partial \varphi_{se}}{\partial x} \right) = j^{Li} \left( \frac{1}{\sigma^{eff}} + \frac{1}{\kappa^{eff}} \right)$  |
| Ohm's law in the solution phase         | $\frac{\partial}{\partial x} \left( K_D^{eff} \frac{\partial \varphi_e}{\partial x} \right) + \frac{\partial}{\partial x} \left( K_D^{eff} \frac{\partial \ln \varphi_e}{\partial x} \right) + j^{Li} = 0 \quad \frac{\partial \varphi_e}{\partial x} \Big _{x=0} = \frac{\partial \varphi_e}{\partial x} \Big _{x=L} = 0$   |  |
| Butler-Volmer equation                  | $j^{Li} = a_s i_0 \left\{ \exp \left[ \frac{\alpha_a F}{RT} (\eta - \eta_{SEI}) \right] - \exp \left[ - \frac{\alpha_c F}{RT} (\eta - \eta_{SEI}) \right] \right\}$ $\eta = \varphi_s - \varphi_e - U$   | $j^{Li} = \frac{a_s i_0 F}{RT} (\varphi_{se} - U)$   |
| Ion concentration in the solution phase | $\frac{\partial (\varepsilon_e c_e)}{\partial t} = \frac{\partial}{\partial x} \left( D_e^{eff} \frac{\partial c_e}{\partial x} \right) + \frac{1-t^0}{F} j^{Li}$ $\frac{\partial c_e}{\partial t} \Big _{x=0} = \frac{\partial c_e}{\partial t} \Big _{x=L} = 0$  |  |
| SOC definition                          | $SOC = \left[ \frac{1}{L} \int_0^L \frac{(c_{s,ave} - c_{s,max} \cdot Stoi0)}{c_{s,max} \cdot (Stoi100 - Stoi0)} \cdot dx \right] \cdot 100\%$   |  |

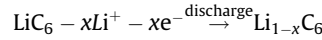
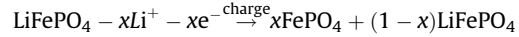
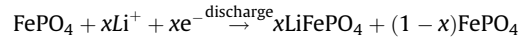
## 2. Model

### 2.1. Modeling principles

Working principle of cells with LFP cathodes is similar to that of LiMnO<sub>4</sub> (LMO) or LiNi<sub>x</sub>Mn<sub>y</sub>Co<sub>1-x-y</sub>O<sub>2</sub> (NMC) cathode. Ion transport and intercalation as well as deintercalation are described using electrochemical kinetics, mass and charge balance and Ohm's law. The LMO cells are extensively analyzed in a previous work [19] and summarized in Table 1 and value of the parameters are listed in Table 2. The only difference between the LMO/NMC and LFP chemistry is the mechanism of ions intercalation and deintercalation in solids that are described below.

For cells made of carbon anode and LFP cathode, lithium ions are transported from anode to cathode during discharging, and

vice versa. Oxidation and reduction processes taking place in electrodes are described as follows,



When LFP cells are charged or discharged, there are transitions between single phase and two-phase dependent upon ion

**Table 2**

List of model parameters (a: Manufacture; b: Extracted from model validation; c: Estimated).

| Parameter  | Negative electrode   | Separator            | Positive electrode   |                      | unit                              |
|--|--|----------------------|----------------------|----------------------|-----------------------------------|
|  |  |                      | $\alpha$ phase       | $\beta$ phase        |                                   |
| Electrode plate area, $A$                                    | 13.3   |                      | 12.6                 |                      | cm <sup>2</sup> a                 |
| Thickness, $\delta$  | $65 \cdot 10^{-4}$   | $16 \cdot 10^{-4}$   | $162 \cdot 10^{-4}$  |                      | cm a                              |
| Particle radius, $R_s$                                       | $8.5 \cdot 10^{-4}$  |                      | $12.5 \cdot 10^{-4}$ |                      | cm a                              |
| Active material volume fraction, $\varepsilon_s$             | 0.62   |                      | 0.56                 |                      | a                                 |
| Polymer phase volume fraction, $\varepsilon_p$               | 0.017  | 0.5                  | 0.065                |                      | a                                 |
| Conductive filler volume fraction, $\varepsilon_f$           | 0.013  |                      | 0.025                |                      | a                                 |
| Porosity, $\varepsilon_e$                                    | 0.35   | 0.5                  | 0.35                 |                      | a                                 |
| Average electrolyte concentration, $c_e$                     | 0.0123   | 0.0123               | 0.0123               |                      | mol cm <sup>-3</sup> a            |
| Maximum solid phase concentration, $c_{s,max}$               | 0.042  |                      | 0.012                |                      | mol cm <sup>-3</sup> c            |
| Diffusion coefficient in solid, $D_s$                        | $2.20 \cdot 10^{-9}$   |                      | $4.27 \cdot 10^{-9}$ | $2.56 \cdot 10^{-8}$ | cm <sup>2</sup> s <sup>-1</sup> b |
| Diffusion coefficient in electrolyte, $D_e$                  | $2.60 \cdot 10^{-6}$   | $2.60 \cdot 10^{-6}$ | $2.60 \cdot 10^{-6}$ |                      | b                                 |
| Limitation concentration ( $c_{s,\alpha\beta} / c_{s,max}$ ) |  |                      | 0.064                | 0.8                  | b                                 |
| Stoichiometry at 0% SOC, $Stoi_0$                            | 0.1155   |                      | 0.9059               |                      | b                                 |
| Stoichiometry at 100% SOC, $Stoi_{100}$                      | 0.6958   |                      | 0.0064               |                      | b                                 |
| Equilibrium potential of positive electrode                  | $3.4245 + 0.85 \exp(-400y^{1.3}) - 17 \exp(-0.98y^{-14})$ , $y = c_{s,surf} / c_{s,max}$   |                      |                      |                      |                                   |
| Equilibrium potential of negative electrode                  | $(0.1011 - 0.04 \tanh(13.76x - 8.4))(x \leq 1) - 252.707$<br>$(x - 0.854)^3 (x > 0.854 \ \& \ x \leq 1) + (0.0523 - 0.05275 \tanh(14.05x - 0.856))$<br>$(x \leq 0.4) + (71.43 (x - 0.085)_2)(x \leq 0.085)$ ; $x = c_{s,surf} / c_{s,max}$ |                      |                      |                      |                                   |

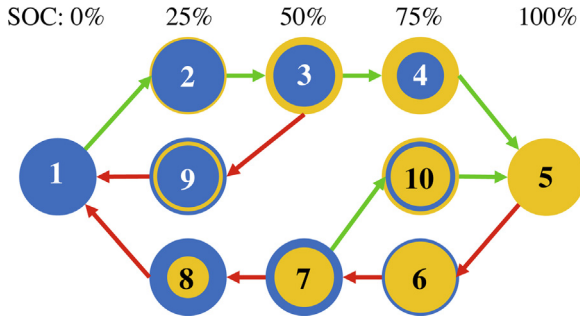


**Fig. 1.** Juxtaposition of phases in LFP particles at different SOC levels with different cycling history: Green and red arrows for discharging and charging, respectively; blue and yellow color for  $\beta$  and  $\alpha$  phase. (For interpretation of the references to colour in this figure legend, the reader is referred to the web version of this article.)

concentration inside of particles. This transition versa is schematically depicted in Fig. 1. When a cell of 100% SOC is discharged, lithium ions transported from anode to cathode diffuse into LFP particles, which creates a single phase called  $\alpha$  phase, as shown in the particle 5 of Fig. 1. While the discharging process continues, the ion concentration on the surface of the particles get increased and saturated with a value,  $c_{s,\alpha\beta}$ , then creates a new phase called  $\beta$  phase. The concentration in  $\beta$  phase is equal to or larger than the maximum value of  $c_s, \beta_{\alpha}$ . With more ions inserted and diffused in the particle, the region of  $\alpha$  phase decreases, while the region of  $\beta$  phase grows, and the region where two phases coexist is called a two-phase region shown with particle 6 to 8. As discharging continues, the cell finally reaches a low SOC,  $\alpha$  phase gets depleted and only  $\beta$  phase is present, so a single-phase exists, which is called a single phase region of  $\beta$  as shown in particle 1. This two-phase dynamics can be described using a two-phase transition and the moving interface [8].

When the cell is sufficiently rested, it can be assumed that there is no gradient of the ion distribution in a particle. Ion distribution for LFP particles is determined by the juxtaposition of the two phases that depends on the cycling history of the cell. When a battery that has an initial value of 0% SOC is charged to 50% SOC, the particle in the shell finds itself in  $\beta$  phase, but in the core  $\alpha$  phase, as shown the step 1  $\rightarrow$  2  $\rightarrow$  3 in Fig. 1. Conversely, the particle becomes  $\alpha$  phase in the shell and  $\beta$  phase in the core, as shown with step 5  $\rightarrow$  6  $\rightarrow$  7, when the battery is discharged from 100% SOC to 50%. Besides juxtapositions, the number of layers at the same SOC can be different. When being discharged from 50% to 25% SOC, the particles might have two layers with  $\beta$  on the surface as shown with step 7  $\rightarrow$  8, or three layers as shown with step 3  $\rightarrow$  9. Consequently, multiple layers can be formed during charging and discharging.

When particles are in single phase, as shown in Fig. 1, the ion diffusion within particles is simply described using Fick's law of diffusion. The governing equation of ion concentration  $c_s$  in a particle with a radius of  $R_s$  and the boundary conditions on the surface of the particle are as follows,

$$\begin{aligned} \frac{\partial c_s}{\partial t} &= \frac{D_s}{r^2} \frac{\partial}{\partial r} \left( r^2 \frac{\partial c_s}{\partial r} \right) \\ D_s \frac{\partial c_s}{\partial r} \Big|_{r=0} &= 0, \\ D_s \frac{\partial c_s}{\partial r} \Big|_{r=R_s} &= \frac{-j^{Li}}{a_s F} \end{aligned} \quad (2)$$

where  $r$  is the radial coordinate,  $\varepsilon_s$  is the volume fraction of active material and  $D_s$  is the solid phase diffusion coefficient.  $j^{Li}$  is the current density, whose sign is positive when Li ions are transported from solid to electrolyte and negative when Li ions are transported

from electrolyte to solid.  $a_s$  is the interfacial surface area calculated from  $3 \varepsilon_s / R_s$ , and  $F$  is the Faraday's constant. The diffusivity of  $\alpha$  and  $\beta$  phase is different from each other, which results in different values of the diffusion coefficient dependent on the phase of the particle.

When two layers are formed, as shown with steps from 2 to 4 and 6 to 8 in Fig. 1, Fick's law can be extended to describe ion diffusion, where boundary conditions are different. When a fully charged battery is being discharged, the ion concentration increases on the surface of the particle, and creates  $\beta$  phase. The interface between two phases moves into the center of the particle. Correspondingly, the governing equations for ion concentration in the two-regions are as follows,

$$\begin{aligned} \frac{\partial c_s}{\partial t} &= \frac{D_{s,\alpha}}{r^2} \frac{\partial}{\partial r} \left( r^2 \frac{\partial c_s}{\partial r} \right), \\ D_{s,\alpha} \frac{\partial c_s}{\partial r} \Big|_{r=0} &= 0, \end{aligned} \quad (3)$$

$$\begin{aligned} \frac{\partial c_s}{\partial t} &= \frac{D_{s,\beta}}{r^2} \frac{\partial}{\partial r} \left( r^2 \frac{\partial c_s}{\partial r} \right), \\ D_{s,\beta} \frac{\partial c_s}{\partial r} \Big|_{r=R_s} &= \frac{-j^{Li}}{a_s F}, \end{aligned} \quad (4)$$

The location of the moving interface between layer 1 and layer 2, as shown in (a) of Fig. 2, can be calculated based on ion concentration. Assuming the moving interface between the two regions is driven only by the concentration gradient of ions that are distinct in the two phases, the governing equation for the moving interface of the mass balance can be rewritten as,

$$(c_{s,\beta\alpha} - c_{s,\alpha\beta}) \frac{dr_0}{dt} = D_{s,\alpha} \frac{\partial c_s}{\partial r} \Big|_{r=r_0} - D_{s,\beta} \frac{\partial c_s}{\partial r} \Big|_{r=r_0+}. \quad (5)$$

When a fully charged battery is being discharged, there is a state that  $\beta$  phase generated on the surface as shown in particle 7. After a period when discharging stops and then a charging current is applied, the ion concentration on the surface of LFP particles decreases and  $\alpha$  phase is created, which results in three layers, as shown with particle 10 in Fig. 1, and more details are shown in (b) of Fig. 2. The ion concentration in multiple layers can be described by modified Fick's law and the following assumptions are made: the ion concentration in Layer 3 and the inner layers does not change, and the location of the interface between Layer 2 and Layer 3 does not moving during cell operation,

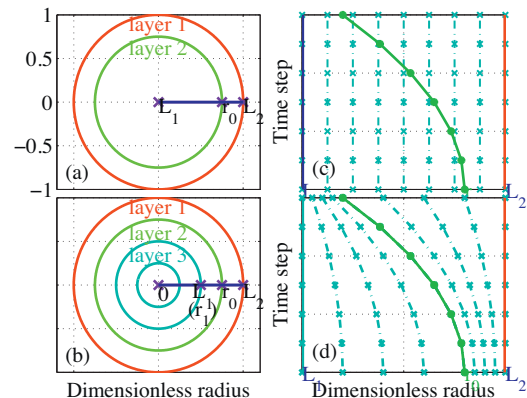


**Fig. 2.** Fixed and variable finite difference space grid.

$$\begin{aligned} \frac{\partial c_s}{\partial t} &= \frac{D_{s,\beta}}{r^2} \frac{\partial}{\partial r} \left( r^2 \frac{\partial c_s}{\partial r} \right), \\ D_{s,\beta} \frac{\partial c_s}{\partial r} \Big|_{r=r_1} &= 0 \end{aligned} \quad (6)$$

$$\begin{aligned} \frac{\partial c_s}{\partial t} &= \frac{D_{s,\alpha}}{r^2} \frac{\partial}{\partial r} \left( r^2 \frac{\partial c_s}{\partial r} \right) \\ D_{s,\alpha} \frac{\partial c_s}{\partial r} \Big|_{r=R_1} &= \frac{-j^{Li}}{\alpha_s F} \end{aligned} \quad (7)$$

$$(c_{s,\alpha\beta} - c_{s,\beta\alpha}) \frac{dr_0}{dt} = D_{s,\beta} \frac{\partial c_s}{\partial r} \Big|_{r=r_0} - D_{s,\alpha} \frac{\partial c_s}{\partial r} \Big|_{r=r_0+}, \quad (8)$$

where  $r_0$  is the location of the interface between layer 1 and 2, while  $r_1$  is the location of the interface between layer 2 and 3, as shown in (b) of Fig. 2.

## 2.2. Numerical method

The equations describing ion diffusion are partial differential equations (PDE) that can be solved using the finite difference method in both time domain and space domain. To achieve high numerical accuracy and better stability, the Crank–Nicholson implicit method is employed. The location of the boundary is a function of both time and space, which is called ‘moving boundary’ problem or Stefan problem. This problem can be solved by either fixed finite difference grid method or variable space grid method. The appropriateness of two methods are studied with respect to their scheme.

For the fixed finite difference method, at different time steps the moving boundary  $r_0$  is plotted in green curve, and the fixed boundary of L1 and L2 are plotted in blue and red lines as (c) of Fig. 2 shows, where the boundary is not always on the grid points, but is located between two grid points. So the space derivatives on the moving boundary need to be modified.

An alternative method is to modify the space grid. The variable space grid [20] and the moving boundary are shown in (d) of Fig. 2. With the following transformation, two new space coordinates are created as,

$$x = \frac{r - L_2}{r_0 - L_2}, \text{ for layer 1,} \quad (9)$$

$$y = \frac{r - L_1}{r_0 - L_1}, \text{ for layer 2,} \quad (10)$$

The moving boundary is always on the grip point of  $x = 1$  at any time instant. According to Eq. 4.21 in [20], the left term in the PDEs can be transformed from  $r$  domain to  $x$  and  $y$  domain for the cell and the core, respectively,

$$\begin{aligned} \left( \frac{\partial c_s}{\partial t} \right)_r &= \left( \frac{\partial c_s}{\partial x} \right)_t \left( \frac{\partial x}{\partial t} \right)_x + \left( \frac{\partial c_s}{\partial t} \right)_x, \\ \frac{dx}{dt} &= \frac{\partial x}{\partial r_0} \frac{dr_0}{dt} \end{aligned} \quad (11)$$

The governing equations and the boundary conditions in (3) to (5) and (6) to (8) can be transformed to (12) to (14),

$$(r_0 - L_1)^2 \frac{\partial c_s}{\partial t} = D_{s,y} \frac{\partial^2 c_s}{\partial y^2} + (r_0 - L_1) \left( y \frac{dr_0}{dt} + \frac{2D_{s,y}}{L_1 + y(r_0 - L_1)} \right) \frac{\partial c_s}{\partial y} \quad (12)$$

$$D_{s,y} \frac{\partial c_s}{\partial y} \Big|_{y=0} = 0$$

$$(r_0 - L_2)^2 \frac{\partial c_s}{\partial t} = D_{s,x} \frac{\partial^2 c_s}{\partial x^2} + (r_0 - L_2) \left( x \frac{dr_0}{dt} + \frac{2D_{s,x}}{L_2 + x(r_0 - L_2)} \right) \frac{\partial c_s}{\partial x} \quad (13)$$

$$\frac{D_{s,x}}{(r_0 - L_2)} \frac{\partial c_s}{\partial x} \Big|_{x0} = \frac{-j^{Li}}{\alpha_s F}$$

$$(c_{s,yx} - c_{s,xy}) \frac{dr_0}{dt} = \frac{D_{s,x}}{r_0 - L_2} \frac{\partial c_{s,x}}{\partial x} \Big|_{x=1} - \frac{D_{s,y}}{r_0 - L_1} \frac{\partial c_{s,y}}{\partial r} \Big|_y = 1 \quad (14)$$

where the sub-index of diffusion coefficient  $D_s$  and concentration  $c_s$  represents the phase of the layer,  $x$  for Layer 1 (the shell) and  $y$  for layer 2.

## 2.3. Order reduction of the model

The equations introduced in Section 2.2 are partial differential equations, the order of which needs to be reduced to find a viable solution for real time applications. One of the order reduction methods used for ion concentrations in NMC cells is the polynomial approach. When there exists single  $\alpha$  or  $\beta$  phase, the approach applied to NMC cells can be used, but the coexistence of two-phase in particles requires modification of the method considering the number of layers.

Two phase states in the particles during discharging process are approximated with a core of  $\alpha$  phase and a shell of  $\beta$  phase. The concentration in  $\alpha$  phase is assumed to be a biquadratic function of spatial position, while concentration in  $\beta$  phase is assumed to be a quadratic function of spatial coordinate.

For the inner layer of  $\alpha$  phase,

$$\begin{aligned} c_s(r, t) &= a(t) + b(t) \cdot \left( \frac{r^2}{r_0^2} \right) + d(t) \cdot \left( \frac{r^4}{r_0^4} \right), \\ \frac{1}{r} \frac{\partial c_s}{\partial r} \Big|_{r=0} &= 0 \\ c_s(r_0, t) &= c_{s,\alpha\beta} \end{aligned} \quad (15)$$

where the coefficients,  $a(t)$ ,  $b(t)$  and  $d(t)$  denote the coefficients that are a function of time, and  $r_0$  is the current location of the interface between the outer two phases and  $r_1$  is the current location of the interface between the inner two phases, which is assumed to be constant.

Similar to the reduction method introduced in [19], the three coefficients are obtained by introducing three variables, volume-averaged concentrations,  $c_{s,ave}$ , volume-averaged concentration fluxes,  $q_{ave}$ , and surface concentrations,  $c_{s,surf}$ , which is a constant,

$$\begin{aligned} a(t) &= \frac{39}{4} c_{s,surf} - 3q_{ave} R_s - \frac{35}{4} c_{s,ave} \\ b(t) &= -35c_{s,surf} + 10q_{ave} R_s + 35c_{s,ave} \\ d(t) &= \frac{105}{4} c_{s,surf} - 7q_{ave} R_s - \frac{105}{4} c_{s,ave} \end{aligned} \quad (16)$$

Combined with (15) and (16), the three equations of volume-averaged concentration, volume-averaged concentration flux and surface concentration above result in as following,

$$\begin{aligned} \frac{d}{dt} c_{s,ave} - 3 \frac{D_s}{r_0^2} (35(c_{s,surf} - c_{s,ave}) - 8q_{ave} r_0) &= 0 \\ \frac{d}{dt} q_{ave} + \frac{1}{2} \frac{D_s}{r_0^3} (60q_{ave} r_0 - 45)(35(c_{s,surf} - c_{s,ave}) - 8q_{ave} r_0) &= 0 \end{aligned} \quad (17)$$

For the outer layer of  $\beta$  phase,

$$\begin{aligned} c_s(r, t) &= a(t) + b(t) \cdot (r - r_0) + d(t) \cdot (r - r_0)^2 \\ D_s \frac{\partial c_s}{\partial r} \Big|_{r=R_s} &= \frac{-j^{Li}}{\alpha_s F} \\ c_s(r_0, t) &= c_{s,\beta\alpha} \end{aligned} \quad (18)$$

where the coefficients of  $a(t)$ ,  $b(t)$  and  $d(t)$  are also a function of time. The three coefficients are derived from three new variables, averaged ion concentration in  $\beta$  phase,  $c_{s,ave}$ , ion

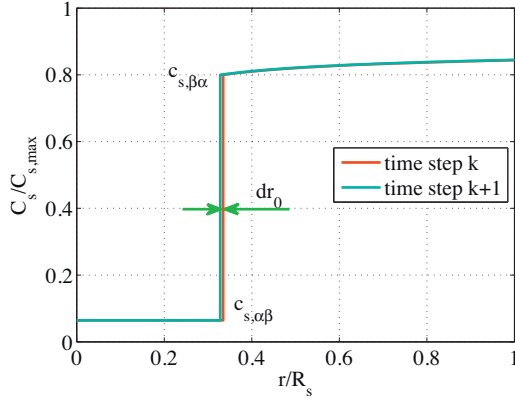


Fig. 3. Mass conservation in the control volume.

concentration on the particle surface,  $c_{s,surf}$ , and the location of the interface,  $r_0$ .

The averaged ion concentration in  $\beta$  phase can be obtained as,

$$c_{s,ave} = \frac{\int_{r_0}^{r_s} 4\pi r^2 C_s(r, t) dr}{4\pi r^2} = a(t) + b(t) * k_1 + d(t) * k_2$$

$$k_1 = \frac{3}{4} \left( \frac{r_s^4 - r_0^4}{r_s^3 - r_0^3} \right) - r_0$$

$$k_2 = \frac{3}{5} \left( \frac{r_s^5 - r_0^5}{r_s^3 - r_0^3} \right) - \frac{3}{2} r_0 \left( \frac{r_s^4 - r_0^4}{r_s^3 - r_0^3} \right) + r_0^2.$$
(19)

At the interface where  $r = r_0$ , the concentration of  $\beta$  phase is equal to the constant of  $c_{s,\beta\alpha}$ , which yields,

$$c_{s,\beta\alpha} = c_s(r, t)_{r=r_0} = a(t).$$
(20)

On the surface of the particle, where  $r = r_s$ , the concentration is equal to the variable,  $c_{s,surf}$ , which yields,

$$c_{s,surf} = c_s(r, t)_{r=r_s} = a(t) + b(t) \cdot k_3 + d(t) \cdot k_4$$

$$k_3 = (r_s - r_0)$$

$$k_4 = (r_s - r_0)^2$$
(21)

So the coefficients of  $a(t)$ ,  $b(t)$  and  $d(t)$  can be replaced with polynomial functions of  $c_{s,ave}$ ,  $c_{s,surf}$ , and  $r_0$ , as shown in following equations,

$$a(t) = c_{s,\beta\alpha}$$

$$b(t) = \frac{(c_{s,surf} - c_{s,\beta\alpha})k_2 - (c_{s,ave} - c_{s,\beta\alpha})k_4}{k_2k_3 - k_1k_4}$$

$$d(t) = \frac{(c_{s,ave} - c_{s,\beta\alpha})k_3 - (c_{s,surf} - c_{s,\beta\alpha})k_1}{k_2k_3 - k_1k_4}$$
(22)

Since the ion concentrations can be substituted using  $c_{s,ave}$ ,  $c_{s,surf}$ , and  $r_0$ , the boundary condition in can also be rewritten as,

$$\frac{(c_{s,surf} - c_{s,\beta\alpha})(k_2 - 2k_1(r_s - r_0)) - (c_{s,ave} - c_{s,\beta\alpha})(2k_3(r_s - r_0) - k_4)}{k_2k_3 - k_1k_4}$$

$$= \frac{-j^{Li}}{a_s F}$$
(23)

It should be noted that the control volume changes when the interface moves, but the charges in the control volume should be conserved, as shown in Fig. 3.

Based on the charge conservation, following equation can be derived using averaged ion concentration,

$$c_{s,ave0}^{k+1} \frac{4}{3}\pi (r_s^3 - (r_0^{k+1})^3) - c_{s,ave0}^k \frac{4}{3}\pi (r_s^3 - (r_0^k)^3)$$

$$+ c_{s,ave1}^{k+1} \frac{4}{3}\pi (r_0^{k+1})^3 - c_{s,ave1}^k \frac{4}{3}\pi (r_0^k)^3 = \frac{-j^{Li}}{a_s F} 4\pi r_s^2.$$
(24)

So, the governing equation for the moving interface can be simplified as,

$$(c_{s,\beta\alpha} - c_{s,\alpha\beta}) \frac{dr_0}{dt} = -D_{s,\beta} \frac{(c_{s,surf} - c_{s,\beta\alpha})k_2 - (c_{s,ave} - c_{s,\beta\alpha})k_4}{k_2k_3 - k_1k_4}$$

$$+ \frac{D_s}{r_0} (35(c_{s,surf} - c_{s,ave}) - 8q_{ave}r_0)$$
(25)

For a particle with three or more layers, the governing equations for ion concentration in the outer layer and the location of the interface are as same as those of two layers, so the same order reduction methods can be applied except the boundary condition at the inner layer. Since the ion concentration at both the boundaries of the inner layer are constant, the polynomial function is defined as,

$$c_s(r, t) = a(t) + b(t) \cdot \left( r - \frac{r_0 + r_1}{2} \right)^2$$

$$c_s(r_1, t) = c_{s,\alpha\beta}$$

$$c_s(r_0, t) = c_{s,\alpha\beta}$$
(26)

Similar to the process from (19) to (22), the average concentration in Layer 2 can be calculated as,

$$\frac{d}{dt} c_{s,ave}$$

$$- 3D_s (c_{s,\alpha\beta} - c_{s,ave}) \frac{(r_0^2 + r_1^2)(r_0 - r_1)}{-r_0r_1(r_0^3 - r_1^3) + \frac{3}{4}(r_0 + r_1)(r_0^4 - r_1^4) - \frac{3}{5}(r_0^5 - r_1^5)}$$

$$= 0.$$
(27)

And the derivatives in (8) also need to be updated,

$$c_{s,ave0}^{k+1} \frac{4}{3}\pi (r_s^3 - (r_0^{k+1})^3) - c_{s,ave0}^k \frac{4}{3}\pi (r_s^3 - (r_0^k)^3)$$

$$+ c_{s,ave1}^{k+1} \frac{4}{3}\pi ((r_0^{k+1})^3 - (r_1^{k+1})^3) - c_{s,ave1}^k \frac{4}{3}\pi ((r_0^k)^3 - (r_1^{k+1})^3)$$

$$= \frac{-j^{Li}}{a_s F} 4\pi r_s^2.$$
(28)

SOC of the cell is defined as the ratio of available charge ( $Q_{releasable}$ ) to the specific charge ( $Q_{max}$ ), which can be calculated based on number of charges,

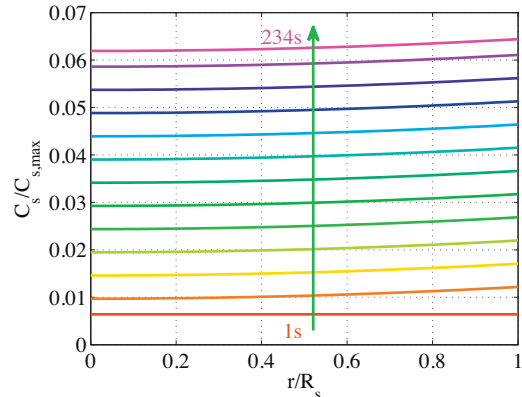


Fig. 4. Ion concentration in a particle with presence of only  $\alpha$  phase during discharging.

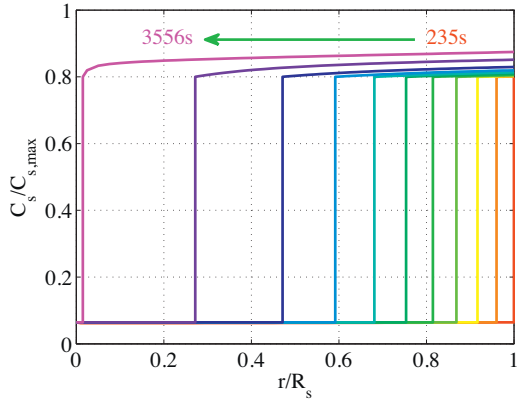


Fig. 5. Ion concentration in a particle at presence of two-phase during discharging.

$$SOC = \frac{Q_{\text{releasable}}}{Q_{\text{max}}} \cdot 100\% \quad (29)$$

The specific charge and the available charge can be calculated based on the averaged ion concentration,

$$\begin{aligned} Q_{\text{releasable}} &= \int_0^L \varepsilon_s \cdot F \cdot c_{s,\text{ave}} \cdot A \cdot dx - \varepsilon_s \cdot F \cdot c_{s,\text{max}} \cdot \text{Stoi}_0 \cdot A \cdot L, \\ Q_{\text{max}} &= \varepsilon_s F c_{s,\text{max}} \cdot (\text{Stoi}_{100} - \text{Stoi}_0) \cdot A \cdot L \end{aligned} \quad (30)$$

where  $A$  is the plate area of the electrode,  $L$  is the thickness of the electrode,  $\text{Stoi}_{100}$  and  $\text{Stoi}_0$  is the stoichiometry at the SOC of 100% and 0%,  $c_{s,\text{max}}$  is the maximum ion concentration in solid particles and  $c_{s,\text{ave}}$  is the volume average ion concentration in solid particles. For a particle with  $m$  layers,  $c_{s,\text{ave}}$  can be calculated as,

$$c_{s,\text{ave}} = \frac{\sum_{i=1}^m (r_{\text{out},i}^3 - r_{\text{in},i}^3) c_{s,\text{ave},i}}{R_s^3}, \quad (31)$$

where  $r_{\text{out}}$  and  $r_{\text{in}}$  is the location of  $i$ th layer's outer and inner boundary.

A reduced order model for ion concentrations in LFP particles during discharging are derived. The PDEs from (3) to (8) that describe ion concentrations in the full order model are replaced by ODEs of (17), (23) to (25), and (27) to (28) using polynomial method, so the calculation time can be drastically reduced. For charging, the interface moves from outer to inner, which is the same as that of discharging. However, the outer layer is  $\alpha$  phase, while the inner layer is  $\beta$  phase. Thus, the same equations can be used but with changed parameters according to the corresponding phase.

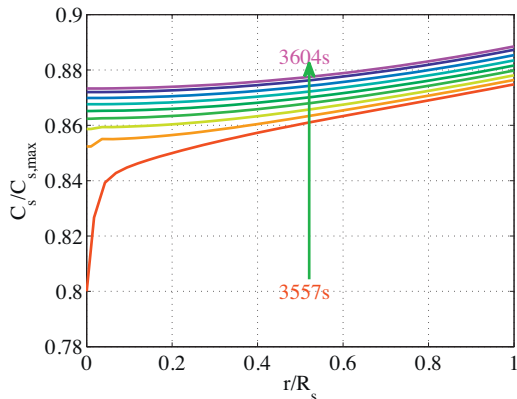


Fig. 6. Ion concentration in a particle at presence of only  $\beta$  phases during discharging.

Rest of submodels for ion concentration in anode particles and the potentials are summarized in Table 1, and more details could be find in [14].

### 3. Results and analysis

A full order shrinking core model is developed at first and then reduced. Then, the reduced model is integrated into the reduced order cell model developed previously [19] that includes mass transport equation in solution phase, Ohm's law for both solution and solid phase, and the Butler Volmer equation. The integrated reduced order model (ROM) is validated against experimental data obtained during galvanostatic discharging and charging with various current rates at constant ambient temperature of 25 °C.

The experiments data is collected for coin cells made of LFP cathode and carbon anode with the equipment of PNE 20 mA. The geometry of the cell and the volume fraction of each material are listed in Table 2. The rated capacity of the cell is 17.284 mAh, which is measured by the following steps: fully charge at 1C in CC/CV mode, rest for 60 min, fully discharge at 1C in CC mode, and rest for 60 min. The discharge capacity is considered as the rated capacity.

#### 3.1. Analysis of and comparison between the FOM and the ROM for a single particle

When a particle is fully charged, only  $\alpha$  phase exists. After a discharging current is applied, changes of the ion concentration distribution take place according three sequences as explained in Section 2.1. At the beginning, particles find themselves in a state where the ion concentration is at the lowest and in only  $\alpha$  phase. As time goes on, more ions are transported to particles and diffuse into inner parts of the particles. The transient behavior of ion concentration is plotted in Fig. 4 as a function of time.

When the ion concentration on the surface of particles reaches the saturation value,  $c_{s,\alpha\beta}$ ,  $\beta$  phase is generated on the surface and continues growing while the discharging current is being applied. As a result, a two-phase is formed inside of particles, where  $\alpha$  phase is in the core and  $\beta$  phase is in the shell.

With more ions inserted into particles, ion concentration continuously increases in both phases, which drives the interface between two phases moving toward the inside of the particle. This transient behavior of the ion concentration at different times is plotted in Fig. 5.

When the interface moves further to the center of the particle,  $\alpha$  phase shrinks and finally disappears. Consequently, only  $\beta$  phase is presented in particles. With discharging continues, ion concentration increases until the ion concentration on the surface of the

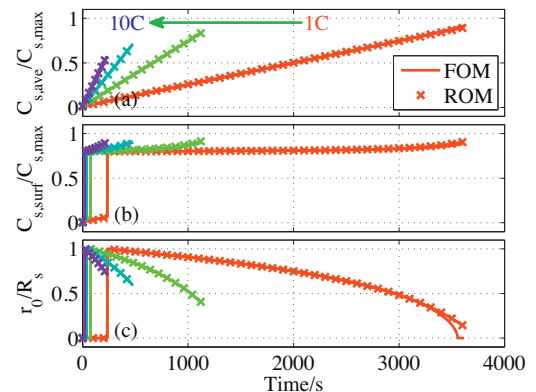


Fig. 7. Comparison of ion distribution in a single particle between FOM and ROM.

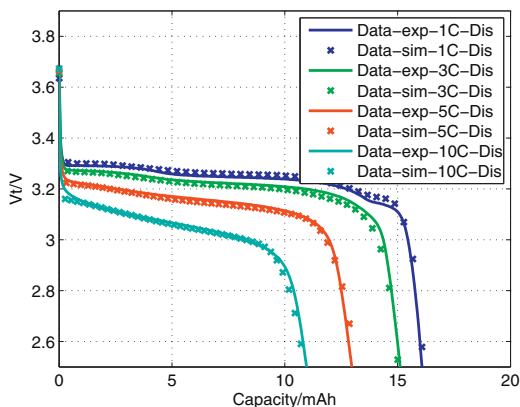


Fig. 8. Comparison of terminal voltage at 1C, 3C, 5C, and 10C during discharging.

particle reaches its maximum limit and then the discharge stops. The ion concentration of  $\beta$  phase is shown in Fig. 6.

Ion concentration in LFP particles can be calculated using FOM. However, due to the large number of meshed grids and multiple layers, the calculation speed is not fast enough for real time application. So the FOM is reduced to a model using the method introduced in Section 2.3. The accuracy and calculation time of the ROM is compared to those of FOM in this section, where constant discharging current rates, 1C, 3C, 5C, and 10C are applied to a single particle with 100% initial SOC. Average ion concentration in the particle, ion concentration at particle surface, and location of the moving interface are plotted in (a), (b), and (c) of Fig. 7. The average concentration of the FOM is the exactly same as that of the ROM because of charge conservation. Likewise, the ion concentration at particle surface and generation and the movement of the interface of both models is the same except a small discrepancy in the location of the interface at the very end of discharging.

In addition, calculation time of the FOM is dramatically reduced by ROM. The number of grid points for FOM in radial direction is 20 in each layer within one particle, so the size of the matrix is  $40 \times 40$  if the particle has two layers. The FOM takes around 1.05s at 3C discharging rate. The size of the matrix in the ROM is 7 for a two-layer particle. The calculation time of the ROM was 0.05s, which is 1/20 of the FOM calculation time.

After testing the accuracy and calculation time of the ROM for a single particle, the ROM is coupled with other equations in Table 1, so the performance of cells can be simulated. The results of the ROM at different load profiles are analyzed in the following sections.

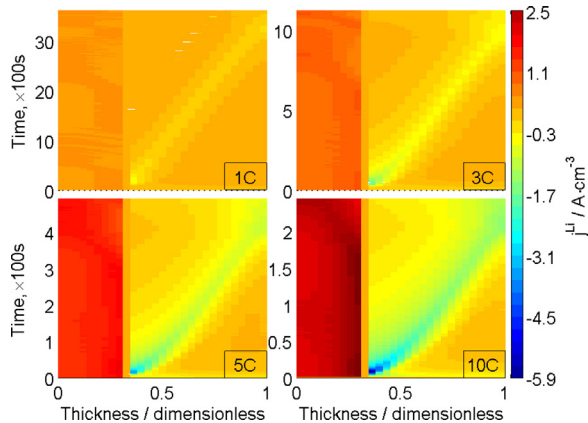


Fig. 9. Current density at 1C, 3C, 5C, and 10C during discharging.

### 3.2. Analysis of the ROM during discharging

In order to analyze performances of the ROM, different discharging current rates are applied as inputs to the model and terminal voltages and SOC as outputs. In addition, internal variables like ion concentrations on surface, current density, and the location of the interface between two layers are calculated. The current rates applied are 1C, 3C, 5C, and 10C, where the initial state of the cell is set to 100% SOC.

Comparisons of simulation results and experimental results of terminal voltage are shown in Fig. 8. The cell is fully charged and particles find themselves in single  $\alpha$  phase. When discharging starts, the terminal voltage drops rapidly. This drop is dependent upon the value of  $\alpha$ .  $\alpha$  is the stoichiometry number that once lithium ion reaches  $\beta$  phase will be generated. The value is tentatively set to be 0.064 in the ROM. In the following region, the terminal voltage drops very slowly, which is caused by the two-phase transition from  $\alpha$  phase to  $\beta$  phase. The difference between the value of  $\alpha$  and  $\beta$  determines the length of the flat voltage that continues. At the end of discharge, the terminal voltage drops rapidly again, which is determined by  $\beta$  phase, and the discharge stops once the terminal voltage reaches 2.5V.

The SOC of the cell is estimated based on average ion concentration in the particles of both composite electrodes. The average ion concentration is calculated based on charge conservation, so during discharging at constant current rate, the SOC decreases linearly from 100% initial value.

The validated model is used to analyze the dependence of ion concentration on locations of particles. When the cell is discharged with a constant current, the current density in the particles near the separator side is high, while the current density near the current collector side is low.

The high current density decreases ion concentration on the surface of particles in the anode side. Conversely, in the cathode side, the current density in the particles near the separator is not always the highest, according to boundary conditions on the surface of the particle.

At the beginning, there exists only  $\alpha$  phase in the cathode side, so the current density is high at the particles near the separator. As discharging continues, the ion concentration in the particles increases. When the concentration reaches  $c_{s,\alpha\beta}$ ,  $\beta$  phase is generated first in those particles located near the separator. Since the diffusivity of  $\beta$  phase is lower than that of  $\alpha$  phase, the ion concentration starts to increase on the surface of the particle and

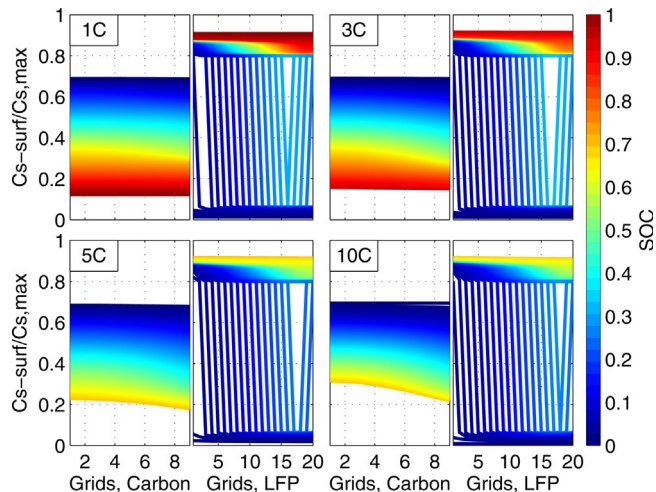


Fig. 10. Simulation results of ion concentrations on the surface particles of both the anode and cathode at 1C, 3C, 5C, and 10C during discharging.

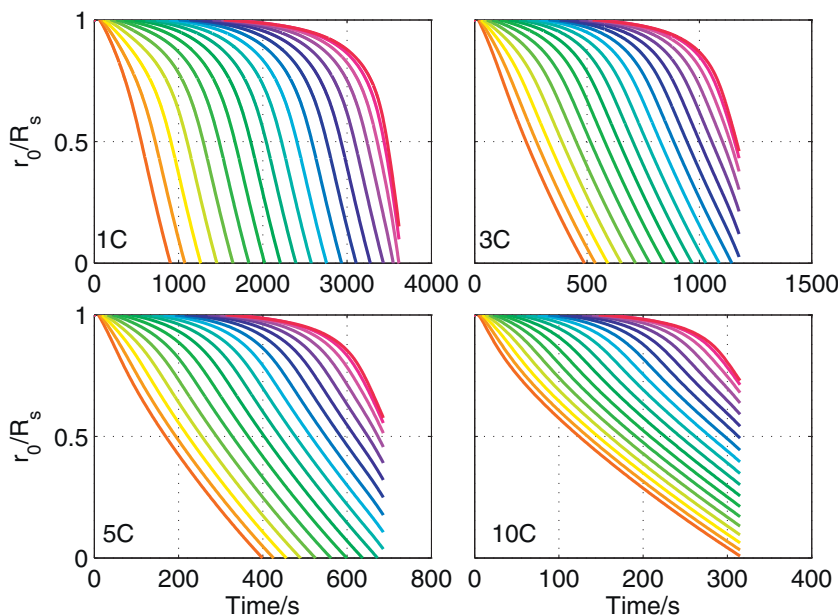


Fig. 11. Simulation results of the moving interface in LFP particles at 1C, 3C, 5C, and 10C during discharging.

then the current density drops at the particle where  $\beta$  phase is generated. While discharging continues, the location of peak current density in the cathode moves from the particles near the separator to the particles near the current collector side, as shown in Fig. 9.

The ion concentration on the surface of the particles at different current rates is shown in Fig. 10. The ion concentration in the anode side decreases during discharging. When the discharging current is high, the concentration gradient in the thickness direction becomes large. Conversely, the ion concentration increases during discharging on the cathode side with the two-phase transition, as shown in Fig. 10.

More details of the two-phase transition and the moving interface between  $\alpha$  and  $\beta$  phase are shown in Fig. 11. At the beginning of discharging, the value of  $r_0/R_s$  is 0, which indicates presence of only  $\alpha$  phase. Once a new phase is generated on the surface of particle, the interface between  $\alpha$  and  $\beta$  phase moves from the surface toward the center of the particle and the value of  $r_0/R_s$  changes from 1 to 0. When  $r_0/R_s$  is 0 again, only  $\beta$  phase is present. At low current rates like 1C, most of the particles find themselves in only  $\beta$  phase at the end of discharging. At high current rate like 10C, all the particles still have two phases and as a result the available specific charge during discharging at a high current rate is lower than that at a low current rate.

### 3.3. Analysis of the ROM during charging

Similar to the analysis of the ROM during discharging, the response of the ROM during charging is analyzed in terms of only terminal voltage and SOC because the others like current density, ion concentration, and location of the interface between two phases have not shown any particular differences in characteristics compared with those of discharging.

The calculated and measured terminal voltage versus available charge are plotted in Fig. 12, where different currents are applied. The simulated results match pretty well with the experimental data.

The larger the charging current rates are, the smaller the charge capacity is. When large current is applied, both concentration overpotential and ohmic overpotential are large, so the terminal

voltage during charging would get to its upper limitation early, which leads to small available charge.

In addition, specific charge during charging is larger than that during discharging even though the current rate is the same. During charging,  $\alpha$  phase is formed in the shell while  $\beta$  phase is in the core. Since the diffusivity of  $\alpha$  phase is better than that of  $\beta$  phase, the concentration gradient in the  $\alpha$  phase is smaller than that of  $\beta$  phase and as a result the concentration overpotential caused by the gradient becomes small and the specific charge during charging is large.

### 3.4. Analysis of the ROM during cycling

When the cell is sufficiently rested, it can be assumed that a steady state is reached, so ions within particles are evenly distributed in the solid particles, which represent a single phase. However, the distribution of the ions in LFP particles is determined by the juxtaposition of the two phases that depends on the cycling history of the cell. For example, when a cell is charged to 50% SOC from an initial 0% SOC, two phases are formed,  $\beta$  phase in the shell and  $\alpha$  phase in the core, as step 1  $\rightarrow$  2  $\rightarrow$  3 shows in Fig. 1. In contrast, when the cell is discharged to 50% SOC from 100% SOC,

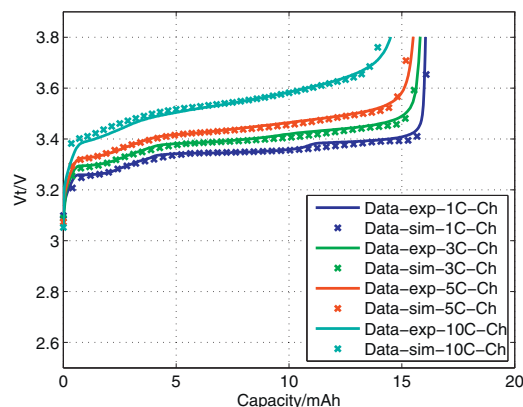
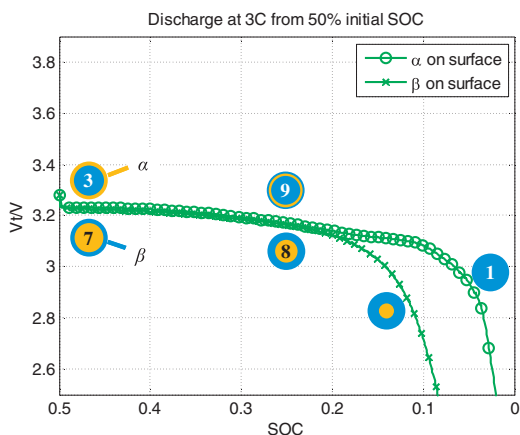


Fig. 12. Comparison of terminal voltage at 1C, 3C, 5C, and 10C charging.



**Fig. 13.** Juxtaposition of phases in LFP particles and the terminal voltage at 3C discharging with 50% of initial SOC and different juxtaposition of the two phases; (a) for 3 → 9 → 1, and (b) for 7 → 8 → 1.

discharged,  $\alpha$  phase and  $\beta$  phase are formed in the shell and in the core of particles, respectively, as the step 5 → 6 → 7 shows.

In addition to juxtapositions of the two phase, the number of layers is also dependent upon cycling history. The number can be different even at the same SOC. When a cell is discharged from an initial state of 50% to 25% SOC, two layers can be formed in particles,  $\beta$  on the surface as the step 7 → 8 show, or three layers as step 3 → 9 shows.

Moreover, cycling history affects cell performance during discharging or charging. For example, the terminal voltage and change of juxtaposition are plotted in Fig. 1. for the case when a cell is discharged with 3C rate from an initial state of 50% SOC. Two kinds of juxtaposition of the two phases in the particles are possible, as shown in step 3 and 7 of Fig. 13, with  $\alpha$  phase or  $\beta$  phase on the surface of the particles, respectively. The terminal voltage of the cell is marked with circles for steps 3 → 9 → 1, and stars for steps 7 → 8 → 1.

When a discharging current is applied,  $\beta$  phase is generated on the surface of the particles that initially have two layers as status 3, so three layers are formed in the particle,  $\beta|\alpha|\beta$  from the shell to the core as status 9 shows. As the discharge continues, the layer of  $\beta$  phase gets enhanced and the interface between the layers moves towards the core, which leads to depletion of the layer of  $\alpha$  phase. Finally,  $\alpha$  phase disappears and there is only one layer of  $\beta$  phase left as status 1 shows, and the interface between the two layers also disappears as (a) in Fig. 14 shows. Different colors are used to

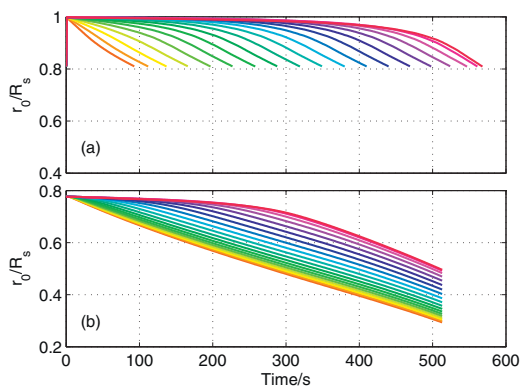


**Fig. 14.** Location of the interface between the two phases in LFP particles at 3C discharging with 50% of initial SOC and different juxtaposition of the two phases; different colors represent particles at different locations in composite cathode. (a) for 3 → 9 → 1, and (b) for 7 → 8 → 1. (For interpretation of the references to colour in the text, the reader is referred to the web version of this article.)

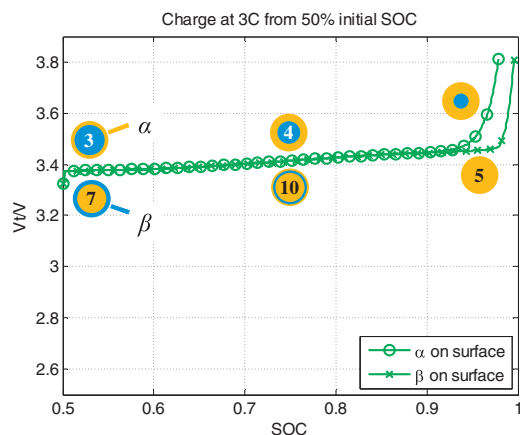


**Fig. 15.** Juxtaposition of the phases in LFP particles and the terminal voltage at 3C charging with 50% of initial SOC and different juxtaposition of the two phases.

indicate the distances of the particles from the separator. The red to purple solid line denote the particles nearest to and farthest from the separator.

When discharge a particle with status of 7, since there is  $\beta$  phase on the surface, the thickness of this layer grows, and the core shrinks as status 8 shows, at the same time the interface moves towards the core as (b) in Fig. 14 shows, and there are two layers in all particles at the end of discharging. However, the total number of charges extracted from the cell with particles of status 3 is more than that of status 7, which matches with the experimental results mentioned in [13] and [12].

In contrast to the discharging process, during the charging process, the total number of charges inserted to the LFP particles of status 3 is less than that of status 7. The terminal voltage and the change of juxtaposition of the phases in LFP particles are plotted in Fig. 15. The location change of the interface at different locations in the cathode is plotted in Fig. 16. At the end of 3C charging from status 3, for the particles near the separator there is only one layer of  $\alpha$  phase left, while for the particles near the current collector there are two layers left. However, charging from status 7, all of the particles reach status 5 with only one layer of  $\alpha$  phase. This explains why more charges are inserted to particles of status 5 than that of status 3.

When discharging or charging a cell from a certain initial SOC, the available charge depends on both current rate and the juxtaposition of the phases in LFP particle. Fig. 17 shows the available charge at different operating conditions. Different colors

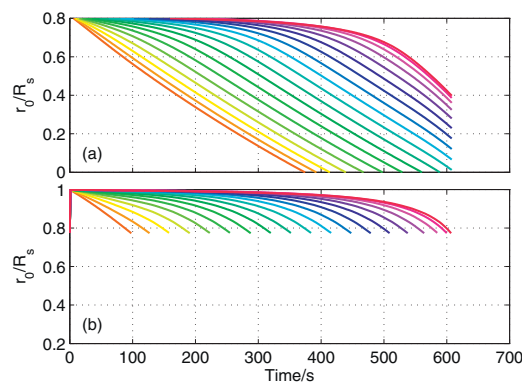


**Fig. 16.** The location of the interface between two phases in LFP particles at 3C charging with 50% of initial SOC and different juxtaposition of the two phases; (a) for 3 → 4 → 5, and (b) for 7 → 10 → 5.

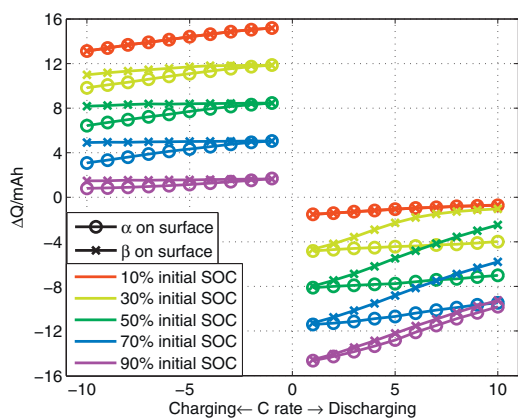


**Fig. 17.** The available charge depending on different current rates, initial SOC, and the juxtaposition of the two phases.

represent different initial SOC, and circles and stars represent cells with  $\alpha$  and  $\beta$  phase on the surface of LFP particles respectively. We can draw the following conclusions from the figure: during discharging the available charge of the cell is larger with  $\alpha$  phase on the surface of LFP particles, while during charging the available charge is larger if there is  $\beta$  phase on the surface of LFP particles; the larger the current rate is, the more severe the path dependence phenomenon is; when the initial SOC is in the range of 30% to 70%, the effect of cycling history is more obvious; the juxtaposition plays a more important role during discharging than during charging.

#### 4. Conclusion

A new reduced order mathematical model for cells with LFP chemistry as cathode and carbon as anode is developed based on electrochemical principles. Particularly, the ion distributions in LFP particles are approximated by a shrinking core model that is described using diffusion equations and simplified using polynomial approximation. The model is capable of representing the three major characteristics of the battery determined by the two-phase transition taking place in LFP particles that include voltage plateau and path dependence.

The developed ROM is validated against experimental data of terminal voltage and SOC during galvanostatic charging and discharging process, and then is used to analyze the major characteristics mentioned above. Major accomplishments of this work are summarized as follows:

1. The model can capture realistic behaviors of LFP cells that includes plateau and path dependence that is otherwise not possible;
2. More available charges are observed during discharging when  $\alpha$  phase is present in the shell at the beginning and during charging when  $\beta$  phase is present.
3. The path dependence is a function of current rates and SOC range. The dependence becomes severe when current rates increase or SOC ranges from 30% to 70%;

4. Performance is more affected by the cycling history during discharging than that during charging.

Future work will include temperature dependence as well as degradation effects.

#### Acknowledgment

This project is funded by LG Chem Ltd. The authors do appreciate the financial support and technical discussions.

#### References

- [1] A.K. Padhi, K.S. Nanjundaswamy, J.B. Goodenough, Phospho-olivines as positive-electrode materials for rechargeable lithium batteries, *Journal of the Electrochemical Society* 144 (Apr 1997) 1188–1194.
- [2] A. Yamada, H. Koizumi, N. Sonoyama, R. Kanno, Phase Change in  $\text{Li}_x\text{FePO}_4$ , *Electrochemical and Solid-State Letters* 8 (2005) A409.
- [3] G. Chen, X. Song, T.J. Richardson, Electron microscopy study of the  $\text{LiFePO}_4$  to  $\text{FePO}_4$  phase transition, *Electrochemical and Solid-State Letters* 9 (2006) A295–A298.
- [4] C. Delmas, M. Maccario, L. Croguennec, F. Le Cras, F. Weill, Lithium deintercalation in  $\text{LiFePO}_4$  nanoparticles via a domino-cascade model, *Nature materials* 7 (2008) 665–671.
- [5] G. Brunetti, D. Robert, P. Bayle-Guillemaud, J. Rouviere, E. Rauch, J. Martin, et al., Confirmation of the domino-cascade model by  $\text{LiFePO}_4/\text{FePO}_4$  precession electron diffraction, *Chemistry of Materials* 23 (2011) 4515–4524.
- [6] K. Weichert, W. Sigle, P.A. van Aken, J. Jamnik, C.B. Zhu, R. Amin, et al., Phase Boundary Propagation in Large  $\text{LiFePO}_4$  Single Crystals on Delithiation, *Journal of the American Chemical Society* 134 (Feb 15) (2012) 2988–2992.
- [7] C. Zhu, L. Gu, L. Suo, J. Popovic, H. Li, Y. Ikuhara, et al., Size-Dependent Staging and Phase Transition in  $\text{LiFePO}_4/\text{FePO}_4$ , *Advanced Functional Materials* 24 (2014) 312–318.
- [8] V. Srinivasan, J. Newman, Discharge model for the lithium iron-phosphate electrode, *Journal of the Electrochemical Society* 151 (2004) A1517–A1529.
- [9] C. Wang, U.S. Kasavajjula, P.E. Arce, A discharge model for phase transformation electrodes: formulation, experimental validation, and analysis, *The Journal of Physical Chemistry C* 111 (2007) 16656–16663.
- [10] U.S. Kasavajjula, C. Wang, P.E. Arce, Discharge Model for  $\text{LiFePO}_4$  Accounting for the Solid Solution Range, *Journal of the Electrochemical Society* 155 (2008) A866.
- [11] I.V. Thorat, T. Joshi, K. Zaghbi, J.N. Harb, D.R. Wheeler, Understanding Rate-Limiting Mechanisms in  $\text{LiFePO}_4$  Cathodes for Li-Ion Batteries, *Journal of the Electrochemical Society* 158 (2011) A1185.
- [12] M. Safari, C. Delacourt, Mathematical Modeling of Lithium Iron Phosphate Electrode: Galvanostatic Charge/Discharge and Path Dependence, *Journal of the Electrochemical Society* 158 (2011) A63–A73.
- [13] V. Srinivasan, J. Newman, Existence of path-dependence in the  $\text{LiFePO}_4$  electrode, *Electrochemical and Solid State Letters* 9 (2006) A110–A114.
- [14] M.A. Roscher, J. Vetter, D.U. Sauer, Cathode material influence on the power capability and utilizable capacity of next generation lithium-ion batteries, *Journal of Power Sources* 195 (2010) 3922–3927.
- [15] M. Safari, C. Delacourt, Mathematical Modeling of Lithium Iron Phosphate Electrode: Galvanostatic Charge/Discharge and Path Dependence, *Journal of the Electrochemical Society* 158 (2011) A63.
- [16] W. Sigle, R. Amin, K. Weichert, P.A. van Aken, J. Maier, Delithiation Study of  $\text{LiFePO}_4$  Crystals Using Electron Energy-Loss Spectroscopy, *Electrochemical and Solid-State Letters* 12 (2009) A151.
- [17] K. Weichert, W. Sigle, P.A. van Aken, J. Jamnik, C. Zhu, R. Amin, et al., Phase boundary propagation in large  $\text{LiFePO}_4$  single crystals on delithiation, *Journal of the American Chemical Society* 134 (Feb 15) (2012) 2988–2992.
- [18] A.V. Churikov, A.V. Ivanishchev, I.A. Ivanishcheva, V.O. Sycheva, N.R. Khasanova, E.V. Antipov, Determination of lithium diffusion coefficient in  $\text{LiFePO}_4$  electrode by galvanostatic and potentiostatic intermittent titration techniques, *Electrochimica Acta* 55 (Mar 1) (2010) 2939–2950.
- [19] X. Li, M. Xiao, S.-Y. Choe, Reduced order model (ROM) of a pouch type lithium polymer battery based on electrochemical thermal principles for real time applications, *Electrochimica Acta* 97 (2013) 66–78.
- [20] J. Crank, *Free and moving boundary problems*, Clarendon Press, Oxford, 1984.